Chemical Science

ROYAL SOCIETY OF CHEMISTRY

EDGE ARTICLE

View Article Online
View Journal

Cite this: DOI: 10.1039/d6sc03303b

All publication charges for this article have been paid for by the Royal Society of Chemistry

Unlocking superior Li^+ transport and anodic compatibility for solid polymer electrolytes by zwitterionic metal–organic filler-mediated Li^+ coordination engineering

Mochun Zhang, †[a] Zhengguang Li, †[b] Yuyan Liu,[c] Bo Hong,[adefg] Fuhua Yang,[adefg] Mengran Wang, *[adefg] Die Liu, *[b] Pingshan Wang [b] and Yanqing Lai*[adefgh]

Residual solvents such as DMF in vinylidene fluoride (VDF)-based solid polymer electrolytes (SPEs) promote lithium salt dissociation but trigger parasitic reactions with the Li metal anode, limiting interfacial stability. Here, we introduce a multifunctional zwitterionic filler (LS) into the poly(vinylidene fluoride-*co*-hexafluoropropylene) (PVDF-HFP) matrix to regulate Li^+ coordination and suppress solvent-induced degradation. The LS filler contains borate groups that compete with DMF for Li^+ binding, weakening Li^+–DMF interactions, while Zn^{2+} sites in its metal–organic cage immobilize $TFSI^-$ anions and establish a Li^+-dominated, weakly coordinated solvation structure. This dual regulation accelerates Li^+ transport and promotes the formation of an inorganic, F- and N-rich solid electrolyte interface (SEI) on the Li metal anode. As a result, the optimized electrolyte (LSPH) delivers a high ionic conductivity of 0.641 mS cm^{-1} and a Li-ion transference number of 0.83 at room temperature, outperforming the filler-free control. The Li|LSPH|Li symmetric cells exhibit a high critical current density of 3.4 mA cm^{-2} and stable cycling for over 1000 h at 1.0 mA cm^{-2}. Furthermore, the Li|LSPH|NCM811 full cells deliver an outstanding discharge capacity of 136.3 mA h g^{-1} at 5C and achieve 70% capacity retention after 1000 cycles at 1C and 4.3 V. This strategy effectively overcomes the trade-off associated with residual solvents in VDF-based electrolytes and advances the development of high-performance solid polymer electrolytes for lithium metal batteries.

Received 21st April 2026
Accepted 20th May 2026

DOI: 10.1039/d6sc03303b

rsc.li/chemical-science

Introduction

Lithium metal is widely regarded as the ideal anode material for next-generation high-energy-density batteries because of its outstanding properties, including an extremely low electrochemical potential (−3.04 V *vs.* SHE) and a very high theoretical specific capacity (3860 mA h g^{-1}).[1–3] Despite these advantages, the practical application of lithium metal anodes with organic liquid electrolytes still faces serious challenges, such as uncontrolled dendrite growth, poor cycling durability, and safety risks.[4,5] A promising approach to address these issues is to replace liquid electrolytes with highly safe and high-performance solid-state electrolytes.[6,7]

Among various solid-state electrolytes, solid polymer electrolytes (SPEs) are particularly attractive because of their mechanical flexibility, interfacial compatibility, ease of processing, and cost-effectiveness.[8–10] Within the family of SPEs, vinylidene fluoride (VDF)-based polymers, including polyvinylidene difluoride (PVDF) and its derivative poly(vinylidene fluoride-*co*-hexafluoropropylene) (PVDF-HFP), have recently emerged as highly promising candidates due to their high mechanical strength and high anti-oxidation ability.[11–14] However, the rigidity of VDF-based polymer matrix exhibits limited Li^+ conductivity and interfacial compatibility, hindering its practical application. To overcome these intrinsic drawbacks, researchers normally improve the ionic conductivity of VDF-based SPEs by retaining a certain amount of solvent (15–

[a]School of Metallurgy and Environment, Central South University, Changsha 410083, P. R. China. E-mail: mengranwang93@163.com; laiyanqing@csu.edu.cn
[b]Department of Organic and Polymer Chemistry, Hunan Key Laboratory of Micro & Nano Materials Interface Science, College of Chemistry and Chemical Engineering, Central South University, Changsha 410083, P. R. China. E-mail: chem-ld@csu.edu.cn
[c]College of Chemistry, Nankai University, Tianjin 300071, P. R. China
[d]Engineering Research Centre of Advanced Battery Materials, The Ministry of Education, Changsha 410083, P. R. China
[e]National Energy Metal Resources and New Materials Key Laboratory, Changsha 410083, P. R. China
[f]National Engineering Research Center of Advanced Energy Storage Materials, Changsha 410083, P. R. China
[g]Hunan Provincial Key Laboratory of Nonferrous Value-Added Metallurgy, Changsha 410083, P. R. China
[h]Yuelushan Center for Industrial Innovation, Changsha 410083, P. R. China
† These authors contributed equally.

25 wt%) in the polymer matrix, such as *N*,*N*-dimethylformamide (DMF) or *N*-methyl-2-pyrrolidone (NMP).[15–17] Residual solvent plasticizes the polymer matrix and dissolves lithium salts, producing solvated $[Li(DMF)_x]^+$ species. Through enhanced salt dissociation and increased carrier concentration, this process improves ionic conductivity. Chen *et al.* showed that incorporating about 15 wt% DMF into PVDF promotes lithium salt dissociation and generates more mobile charge carriers, thereby facilitating Li^+ transport within the polymer matrix.[18] Although excessive residual solvents (DMF or NMP) are beneficial for Li^+ conduction, the strong interaction between Li^+ and DMF/NMP leads to unexpected parasitic reactions with the Li metal anode, destabilizes the anode–electrolyte interface, and shortens cycle life. Therefore, mitigating the impact of residual solvents on the anode is a key focus for the development of VDF-based SPEs.

Recent studies reported several strategies to improve the anodic compatibility of VDF-based electrolytes, such as introducing film-forming additives, immobilizing the residual solvent molecules, or reducing the content of DMF/NMP solvents. Wang *et al.* employed lithium difluoro(oxalato)borate (LiDFOB) as an additive, whose $DFOB^-$ anion forms ion–dipole interactions with NMP, effectively confining NMP and stabilizing the Li anode.[19] Zhou *et al.* introduced 3 Å zeolite fillers to immobilize DMF, weakening the interaction between DMF and Li^+ and improving anodic interfacial stability.[20] More recently, an amorphous polymer system (BPE) with strong Li affinity was incorporated into PVDF to weaken the interaction between Li^+ and DMF, leading to reduced DMF content, which enhances the anodic compatibility.[21] Collectively, these studies demonstrate that residual solvents have detrimental effects on the stability of the anode–electrolyte interface and emphasize the need to mitigate strong Li^+–DMF/NMP interactions or replace them with weakly coordinating solvents. Nevertheless, these strategies face difficulty in simultaneously improving Li^+ conduction and enhancing interfacial stability. Therefore, constructing a stable anodic SEI and optimizing the Li^+ transport environment is essential to further enhance the battery performance.

Herein, we design a multifunctional zwitterionic metal–organic filler (LS) incorporated into the PVDF-HFP matrix to regulate the Li^+ coordination environment and interfacial chemistry. As illustrated in Fig. 1, the borate groups in LS act as cation donor sites that compete with DMF molecules for Li^+ coordination, effectively weakening the strong Li^+–DMF interaction, while the sites within the metal–organic cage serve as anion anchor sites to immobilize free $TFSI^-$ and establish a Li^+-dominated conduction network. This dual-site design promotes fast Li^+ transport and suppresses interfacial side reactions, leading to the formation of a stable F- and N-rich interphase on the lithium metal surface. Benefiting from these effects, the optimized SPE (LSPH) delivers an ionic conductivity of 0.641 mS cm^{-1} and a Li^+ transference number of 0.83 at room temperature, markedly higher than those of the filler-free SPE (PH-Li, 0.456 mS cm^{-1} and 0.47, respectively). Li|LSPH|Li symmetric cells exhibit a high critical current density of 3.4 mA cm^{-2} and stable cycling for over 1000 h at 1.0 mA cm^{-2}, whereas the symmetric cells using PH-Li fails within 300 h. The Li|LSPH|NCM811 full cells demonstrate superior rate capability, with a discharge capacity of 136.3 mA h g^{-1} at 5C, far exceeding the 92.5 mA h g^{-1} of the PH-Li electrolyte, and retain 70% capacity after 1000 cycles at 1C and 4.3 V. These results establish the rational design of multifunctional zwitterionic fillers as a robust and effective pathway to overcome the intrinsic limitations of conventional VDF-based electrolytes for high-performance lithium metal batteries.

Results and discussion

As shown in Fig. 2a, the multifunctional filler LS was synthesized *via* a Schiff base condensation between a rigid metal–organic cage bearing terminal aldehyde groups and a flexible lithium salt segment (LiB5AB) terminated with amino groups. The self-assembly of ligand L with zinc(II) nitrate hexahydrate (1.5 equiv.) was conducted by heating at 65 °C for 12 h in a solvent mixture ($MeOH : CHCl_3 = 1 : 1$, v/v) (Fig. S1).[22] Upon cooling to room temperature, anion metathesis was conducted by adding excess LiTFSI. The intermediate, ligand L and the metal–organic cage were fully characterized by ^1H NMR, ^{13}C NMR, and electrospray ionization mass spectrometry (ESI-MS) (Fig. S2–S8). All signals of ligand L and the metal–organic cage could be well assigned with the aid of 2D correlation spectroscopy (2D-COSY), 2D nuclear Overhauser effect spectroscopy (2D-NOESY) (Fig. S9–S11). The characteristic shifts of the aromatic and pyridyl protons further confirm the successful formation of the metal–organic cage (Fig. S12). The delocalized, negatively charged LiB5AB salt was synthesized following a previously reported method (Fig. S13).[23,24] Its chemical structure was confirmed by ^1H and ^{11}B nuclear magnetic resonance (NMR) spectroscopy, and its molecular weight was determined by mass spectrometry (MS) (Fig. S14). X-ray photoelectron spectroscopy (XPS) confirmed the successful condensation of the cage and LiB5AB, as evidenced by the presence of C=N and C–N bonding signals in the LS filler (Fig. 2b). The LSPH and PH-Li electrolytes were prepared *via* a solution-casting method and formed self-standing films with distinct appearances (yellow for LSPH and white for PH-Li) that exhibited good flexibility (Fig. 2c, d and S15). Compared with PH-Li, LSPH exhibits a flatter surface morphology, which is favourable for improving interfacial contact with lithium metal. Cross-sectional EDS mapping further confirms that Zn and B signals are uniformly distributed throughout the membrane thickness, indicating homogeneous dispersion of the LS filler without noticeable aggregation (Fig. S16). To evaluate the effect of LS content on electrochemical performance, a series of PVDF-HFP-based solid electrolytes with different LS loadings (10–50 wt%) were investigated (Fig. S17). Among them, LSPH-30 exhibited the optimal ionic conductivity and Li^+ transport performance, therefore it was selected for detailed study and denoted as LSPH. For comparison, control electrolytes containing only cage-type units (PH-Cage) or only borate units (PH-LB) were also examined under identical conditions. Although both controls exhibit a modest increase in the Li-ion transference number, no appreciable improvement in ionic conductivity is observed. Specifically, PH-Cage partially enhances $TFSI^-$ immobilization

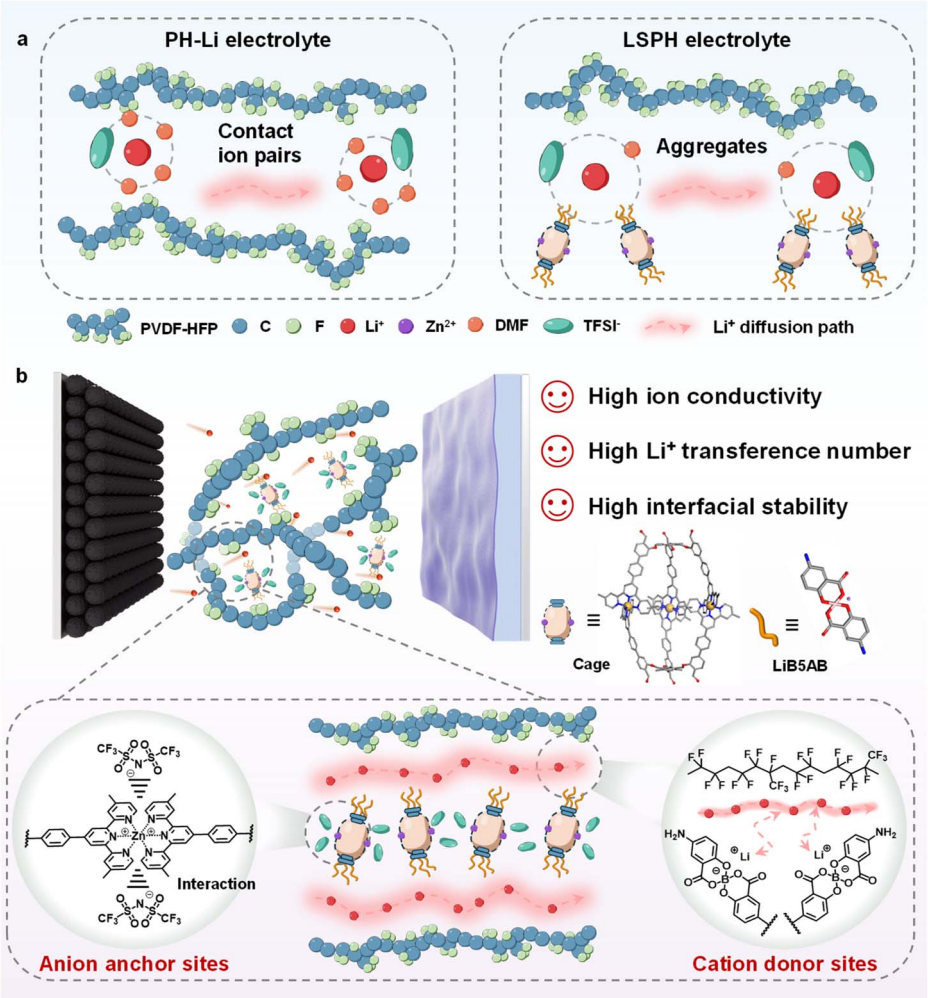

Fig. 1 Schematic illustration of the Li^+ coordination regulation and interfacial stabilization mechanism enabled by the multifunctional zwitterionic filler (LS) in VDF-based solid polymer electrolytes. (a) Comparison of ion coordination structures between the PH-Li and LSPH electrolytes. The incorporation of LS transforms the Li^+ coordination environment from contact ion pairs to aggregated states by anchoring $TFSI^-$ and weakening Li^+–DMF interactions, thereby facilitating Li^+ diffusion. (b) Illustration of the Li^+ transport and interfacial stabilization mechanism in the LSPH electrolyte. The metal–organic cage core containing Zn^{2+} sites function as an anion anchor, while the borate segment acts as a cation donor, synergistically enhancing the ionic conductivity, Li-ion transference number, and interfacial stability.

through Zn^{2+} coordination but fails to modulate Li^+–DMF interactions, whereas PH-LB provides alternative Li^+ coordination sites but lacks the ability to anchor anions. Neither component alone can replicate the dual-regulation effect achieved by the LS filler. In contrast, LSPH simultaneously achieves high ionic conductivity and Li-ion transference number, highlighting the necessity of integrating LS fillers.

X-ray diffraction (XRD) indicated a marked decrease in PVDF-HFP crystallinity upon LS incorporation, which favours faster ion transport (Fig. S18). Mechanical testing showed that LSPH achieved a tensile strength of 8.6 MPa and ~150% elongation at break, compared to only 1.9 MPa and ~65% for PH-Li (Fig. 2e). These enhancements are attributed to the introduction of the LS filler, which reinforces the polymer network and improves the mechanical integrity of the electrolyte. To further assess the role of the LS filler, the electrochemical performance of LSPH was evaluated. As shown in Fig. 2f and S19, the activation energy (E_a) for Li^+ transport in LSPH was 0.167 eV, significantly lower than the 0.221 eV of PH-Li. Additionally, LSPH exhibited a room-temperature ionic conductivity of 0.641 $\times 10^{-3}$ S cm^{-1} and a Li-ion transference number of 0.83, outperforming PH-Li (0.456 $\times 10^{-3}$ S cm^{-1}, $t_{Li^+} = 0.47$) (Fig. 2g). Notably, the residual DMF content in LSPH (4.0 wt%) was significantly lower than that in PH-Li (15.1 wt%). This result indicates that the enhanced ionic conductivity of LSPH cannot be rationalized solely by residual solvent effects and is instead mainly governed by the incorporation of the LS filler (Fig. S20). Although residual DMF acts as a plasticizer that enhances polymer chain segmental mobility, the excessive DMF content in PH-Li (15.1 wt%) compromises mechanical integrity and promotes solvent-induced interfacial degradation during cycling. In contrast, the low residual DMF content in LSPH ensures a more mechanically robust membrane, while the LS filler compensates by providing alternative Li^+ hopping sites to

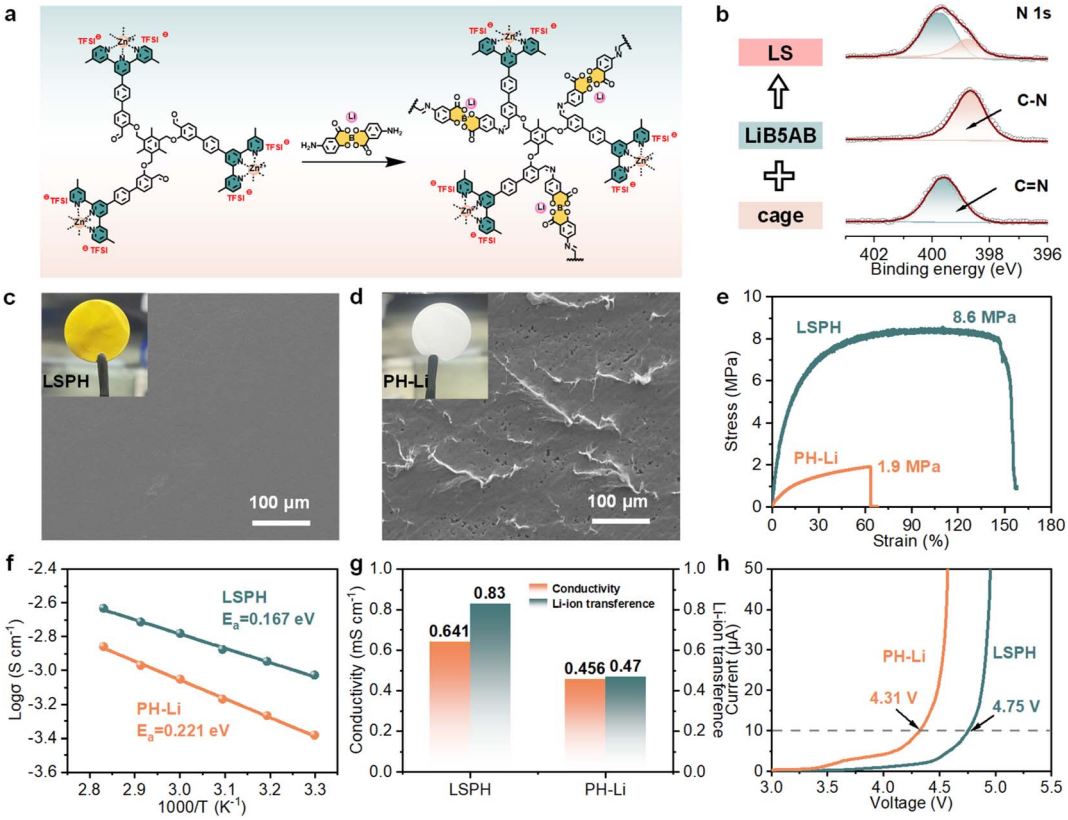

Fig. 2 (a) Schematic of the LS filler synthesis and structure. (b) N 1s XPS spectra of the cage, LiB5AB, and LS, confirming the formation of imine and C–N bonds after condensation. SEM images and optical photographs (inset) of the (c) LSPH and (d) PH-Li electrolyte membranes. (e) Stress–strain curves of the LSPH and PH-Li electrolytes. (f) Arrhenius plots of ionic conductivity for LSPH and PH-Li electrolytes. (g) Room-temperature ionic conductivity and Li^+ transference number of the LSPH and PH-Li electrolytes. (h) Linear sweep voltammetry (LSV) curves of the LSPH and PH-Li electrolytes.

maintain high ionic conductivity. In terms of oxidation stability, as shown in Fig. 2h, linear sweep voltammetry (LSV) revealed an expanded electrochemical stability window from 4.31 to 4.75 V in LSPH, indicating improved compatibility with high-voltage cathodes. This enhancement is mainly attributed to the reduced residual DMF content and LS-mediated regulation of the local coordination environment, which suppresses solvent-related oxidative decomposition. Moreover, the presence of LS modifies the local solvent environment and polymer structure, contributing to the enhanced oxidative stability of the electrolyte.

To elucidate the role of the functional filler LS in modulating the Li^+ coordination structure of SPEs, FT-IR spectroscopy was employed to examine the chemical interactions within the polymer electrolyte membrane (Fig. 3a). In the FT-IR spectrum of LSPH, the characteristic peaks corresponding to C–F, S–N–S, and S–N shifted to lower wavenumbers (1185.3, 1056.9, and 744.2 cm^{-1} respectively), indicating coordination between the LS filler and $TFSI^-$.[21] These shifts highlight the functionality of LS, where Zn^{2+} centres in the cage act as anion receptors that capture $TFSI^-$. Although FT-IR primarily evidences anion coordination, the borate ester groups, serving as Li^+ donors, are expected to compete with DMF for Li^+ coordination. This competitive interaction weakens the Li^+–DMF association and collectively contributes to a looser Li^+ coordination environment, thereby facilitating fast Li^+ conduction. To further substantiate this inference and resolve the coordination evolution, Raman spectroscopy was performed to analyse the specific association states of $TFSI^-$ anions. In LSPH, the S–N–S vibration band of $TFSI^-$ was deconvoluted into signals representing free $TFSI^-$ (741 cm^{-1}), contact ion pairs (CIP, 745 cm^{-1}), and aggregated clusters (AGG, 751 cm^{-1}).[25–27] Upon LS incorporation, the proportions of free $TFSI^-$ and CIP decreased from 39.1% and 52.1% to 15.8% and 42.0%, respectively, while that of AGG increased markedly from 8.8% to 42.2% (Fig. 3b). This shift toward aggregated states confirms that regulating the Li solvation structure may facilitate Li^+ conduction and enhance interfacial stability.[28] To further probe the lithium coordination structure, solid-state nuclear magnetic resonance (ss-NMR) spectroscopy was conducted. In the ^7Li NMR spectrum (Fig. 3c), a downfield shift was observed for LSPH relative to PH-Li, indicating a weakened shielding effect around Li^+ and looser coordination with surrounding ligands.[29] This interpretation was corroborated by the ^{19}F NMR spectrum of $TFSI^-$ (Fig. S21), which revealed that the addition of LS significantly weakened Li^+ coordination with both $TFSI^-$ and DMF, thereby facilitating faster dissociation and ion transport.[30] Binding energy calculations further confirmed this mechanism (Fig. S22). LS exhibits

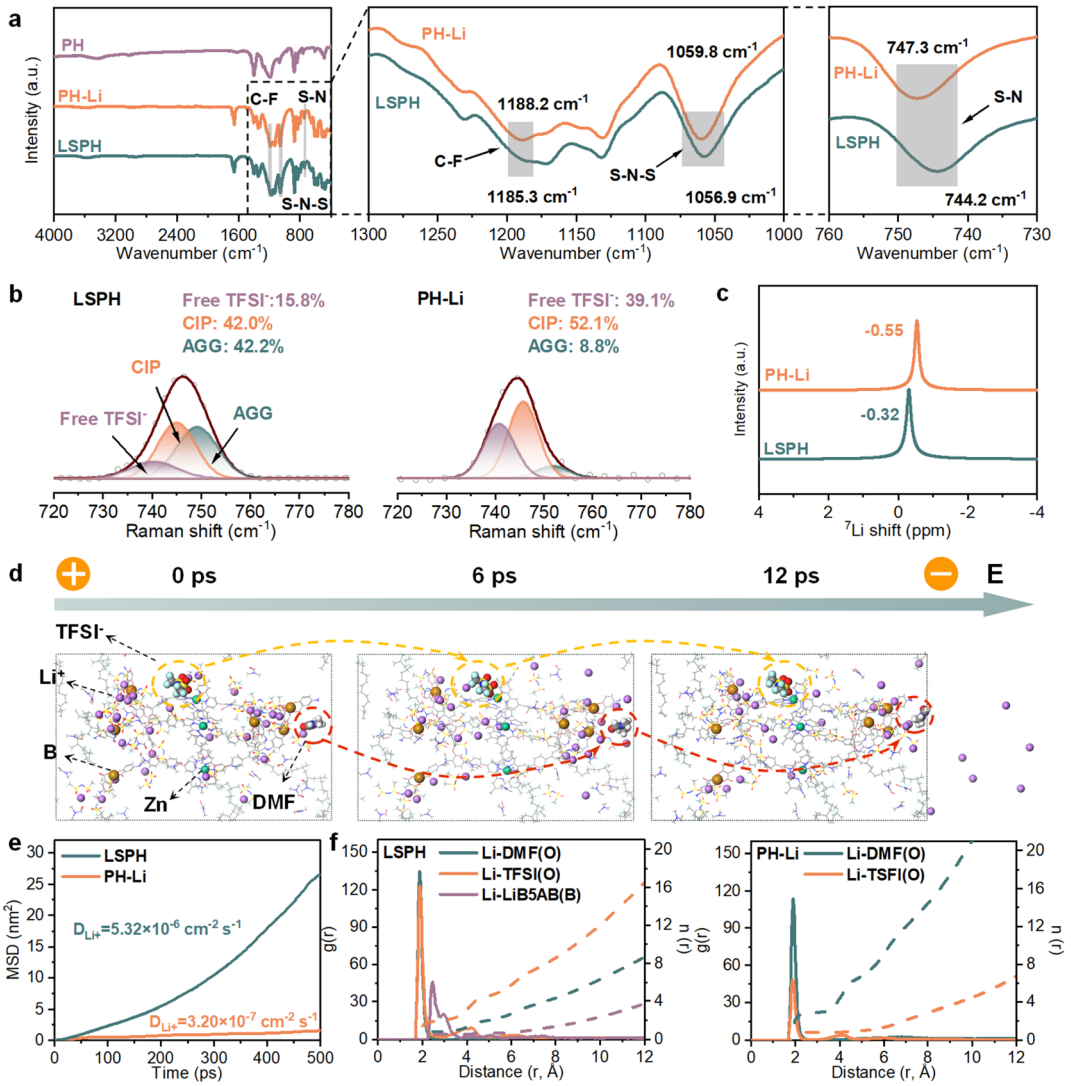

Fig. 3 (a) The FT-IR spectra of PH, PH-Li and LSPH membranes, with an enlarged view of the $TFSI^-$ belonging to PH-Li and LSPH electrolytes. (b) Raman spectra and (c) ^7Li solid-state nuclear magnetic resonance (ss-NMR) spectra of the LSPH and PH-Li electrolytes. (d) The migration model of Li^+, $TFSI^-$ and DMF in LSPH under an applied electric field. (e) Mean square displacement (MSD) of Li^+ and calculated diffusion coefficients. (f) Radial distribution functions (RDFs) showing the coordination environment of Li^+ in the LSPH and PH-Li electrolytes.

stronger binding to $TFSI^-$ than PVDF-HFP or DMF, thereby weakening Li^+–$TFSI^-$ interactions and promoting Li^+ release. Meanwhile, the binding energies of Li^+ with other electrolyte components remain comparable, producing an overall weakly coordinated solvation structure, which is favourable for rapid Li^+ transport. Specifically, the borate ester groups in LS provide weak Li^+ coordination sites (binding energy: −1.593 eV) that compete with DMF (−2.192 eV), while the Zn^{2+} centres anchoring $TFSI^-$ (−4.670 eV). This dual regulation simultaneously enhances Li^+ mobility and suppresses anion transport, which is conducive to achieving a high Li-ion transference number of 0.83.

Based on the coordination structure identified by spectroscopic characterization and binding energy analysis, the diffusion kinetics of Li^+ in the LSPH electrolyte were further assessed *via ab initio* molecular dynamics (AIMD) simulations (Fig. 3d and S23). In LSPH, Li^+ exhibits weaker coordination with surrounding species, which reduces the binding strength and facilitates dissociation. Under the cooperative transport of multiple components, Li^+ achieves much faster migration than in PH-Li. In contrast, in the PH-Li electrolyte, the dissociation of the lithium salt is more difficult, and the transport of Li^+ is relatively slow and irregular within the amorphous PVDF-HFP region. Mean square displacement (MSD) analysis confirmed that the diffusion coefficient in LSPH ($D_{Li^+} = 5.32 \times 10^{-6}$ cm^2 s^{-1}) is more than an order of magnitude higher than that in PH-Li ($D_{Li^+} = 3.20 \times 10^{-7}$ cm^2 s^{-1}), demonstrating a significant enhancement in Li^+ mobility (Fig. 3e). Radial distribution function (RDF) analysis revealed a dominant Li–O peak at 0.20 nm, suggesting that O atoms from DMF and $TFSI^-$ primarily mediate Li^+ transport (Fig. 3f). Compared with PH-Li, the reduced intensity of the Li–O (DMF) contribution in LSPH

indicates weaker Li–DMF coordination, consistent with competitive binding from the borate groups in LS. A secondary Li–B peak at 0.25 nm was attributed to electrostatic interactions with borate anions in LS, which weaken Li^+–$TFSI^-$/DMF binding and facilitate dissociation. These results confirm that the LS filler promotes ion-pair dissociation by restricting $TFSI^-$ mobility and enabling Li^+ hopping *via* multicomponent co-transport, ultimately achieving an enhanced Li-ion transference number and Li^+ conductivity. This mechanistic insight supports the conclusion that LS effectively modulates the coordination structure and dynamics, enabling rapid and stable Li^+ transport in solid polymer electrolytes.

To evaluate the interfacial compatibility between the electrolyte and lithium metal, the lithium plating/stripping behavior and interfacial charge transfer kinetics were examined using Li||Li symmetric cells. As shown in Fig. 4a, the critical current density (CCD) of the Li|LSPH|Li cell reached 3.4 mA cm^{-2}, markedly higher than that of the Li|PH-Li|Li cell (1.7 mA cm^{-2}), indicating enhanced electrochemical stability. The Tafel curves reveal that the exchange current density (j_0) of the Li|LSPH|Li cell (0.283 mA cm^{-2}) is significantly higher than that of the Li|PH-Li|Li cell (0.106 mA cm^{-2}), indicating that the LS filler constructs a more kinetically favourable charge-transfer interface between the lithium metal anode and the electrolyte (Fig. S24). The long-term cycling performance at 1.0 mA cm^{-2} and 0.5 mA h cm^{-2} further demonstrated that the Li|LSPH|Li cell maintained stable cycling for over 1000 h with a low voltage polarization of ~60 mV (Fig. 4b). The enlarged voltage profiles at different stages reveal that the overpotential of LSPH remains consistently low, increasing only slightly from 89 to 140 and 150 mV (at 10 h, 120 h and 240 h), indicating a stable electrode/electrolyte interface throughout prolonged cycling. In contrast, the PH-Li cell exhibits substantially higher overpotentials (90, 630, and 840 mV at the corresponding stages), reflecting severe interfacial degradation and unstable Li plating/stripping behaviour. In contrast, the Li|PH-Li|Li cell showed rapid voltage escalation and a cycle life of less than 300 h due to severe side reactions between DMF and the lithium metal anode.

It is worth noting that although the PH-Li electrolyte intentionally retains a higher amount of residual DMF to enhance polymer flexibility and ionic conductivity, this does not translate into improved interfacial stability. The comparison between PH-Li and LSPH clearly shows that a higher residual DMF content is not positively correlated with long-term interfacial robustness. Instead, excessive Li^+–DMF coordination accelerates solvent-driven side reactions at the lithium metal interface, leading to rapid polarization growth and premature

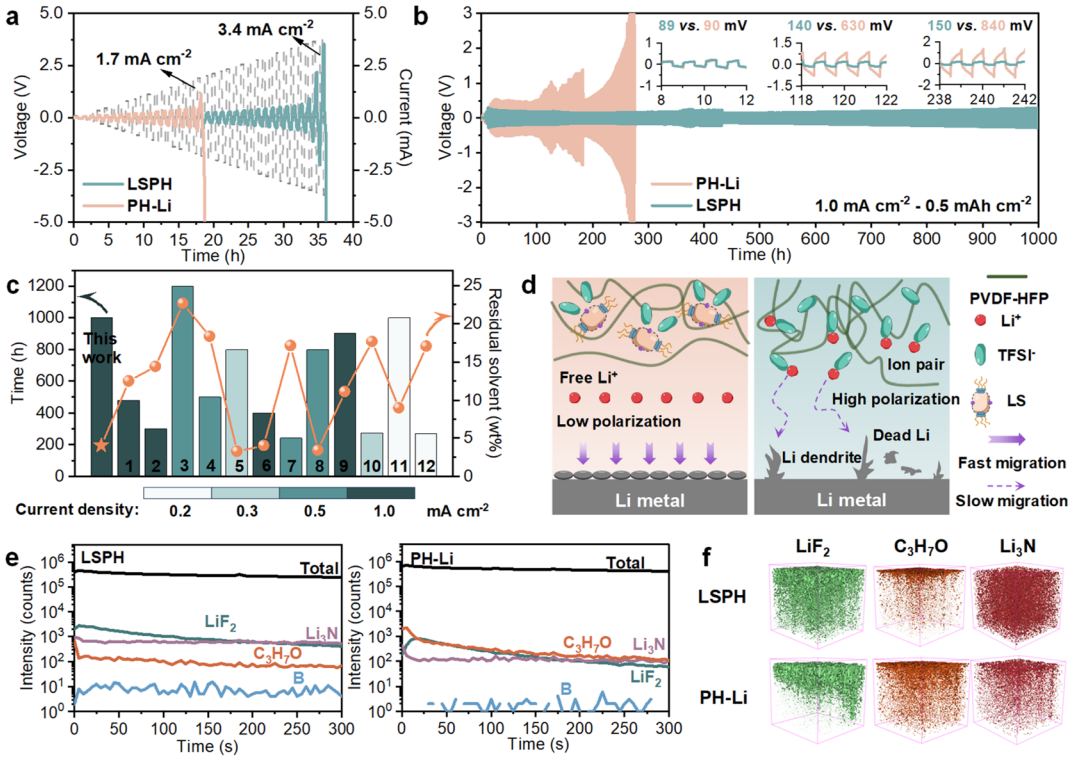

Fig. 4 (a) Critical current density (CCD) of the Li|LSPH|Li and Li|PH-Li|Li symmetric cells with a fixed Li deposition and delamination time of 30 min. (b) Galvanostatic cycling curves of the Li||Li symmetric cells with the PH-Li and LSPH electrolytes. The insets show enlarged voltage profiles at selected time intervals. (c) Performance comparison of the LSPH system with other reported works using VDF-based polymer electrolytes in Li||Li symmetric cells. (d) Schematic illustration of Li deposition and dendrite growth on the lithium metal anode using LSPH (left) and PH-Li (right) electrolytes. (e) Time-of-flight secondary ion mass spectrometry (ToF-SIMS) depth profiling of several secondary ion fragments on the SEI using the LSPH and PH-Li electrolytes. (f) ToF-SIMS 3D reconstruction of the sputtered volume on the SEI using the LSPH and PH-Li electrolytes.

failure. By contrast, the LSPH electrolyte achieves a balanced optimization by reducing the residual DMF content while regulating Li^+ coordination through the LS filler, thereby maintaining sufficient interfacial kinetics without sacrificing long-term stability.

To benchmark the performance, we compared the LSPH electrolyte with other VDF-based electrolytes based on current density, cycle life, and residual solvent content. As depicted in Fig. 4c and Table S1, the LSPH system displayed superior interfacial stability and comprehensive performance, underscoring the advantages of our designed VDF-based electrolyte. Notably, the incorporation of the zwitterionic filler not only mitigates solvent-induced side reactions but also promotes the formation of a stable, inorganic-rich SEI, further enhancing interfacial compatibility and long-term cycling stability.

Post-cycling morphological analysis *via* optical imaging and SEM revealed a smooth and compact lithium surface in the LSPH system, whereas the PH-Li system exhibited deposition with scattered black spots (Fig. S25). SEM images confirmed that the PH-Li cell suffered from dendritic growth and dead lithium accumulation, while the LSPH cell showed a uniform morphology without dendrites. These observations are schematically illustrated in Fig. 4d, highlighting the distinct deposition behaviours. In the PH-Li system, disordered lithium growth is attributed to uneven Li^+ distribution and unstable interfaces. In contrast, the LSPH system supports uniform Li^+ flux and homogeneous deposition, contributing to a stabilized anode interface.[31]

To elucidate the underlying stabilization mechanism, ToF-SIMS was employed to characterize the SEI composition (Fig. 4e). Strong signals of LiF_2^-, Li_3N^-, together with minor B-related contributions, suggest an inorganic-rich SEI in the LSPH system (Fig. 4f).[32] In contrast, the PH-Li system displayed predominantly organic fragments arising from extensive side reactions. Further XPS analysis of the C 1s, F 1s, and Li 1s spectra revealed a compositional gradient within the SEI for both the LSPH and PH-Li systems (Fig. S26).[33] Notably, the F 1s spectrum of LSPH showed increasing LiF intensity with sputtering depth, consistent with the ToF-SIMS results. These findings confirm the formation of a stable SEI enriched in F and N species, which promotes rapid and uniform Li deposition, suppresses dendrite growth, and thereby extends cycling stability and service life. This inorganic-rich interface is attributed to the synergistic effects of LS-mediated solvation regulation and reduced residual DMF content. The weakened Li^+ coordination promotes more $TFSI^-$ decomposition at the interface, generating abundant LiF_2^-, Li_3N^-, while the low DMF content (4.0 wt%) suppresses the formation of organic by-products.

Considering the excellent Li^+ conductivity and favourable interfacial compatibility of the LSPH electrolyte with lithium metal, its application in Li||NCM811 full cells was further explored. Cyclic voltammetry (CV) curves show that the Li|LSPH|NCM811 battery exhibits superior redox reaction reversibility and kinetics (Fig. S27). As shown in Fig. 5a, the Li|LSPH|NCM811 battery exhibited outstanding rate performance, delivering discharge capacities of 197.7, 167.3, 161.2, 158.9, 149.8, 144.8, and 136.3 mA h g^{-1} at current rates of 0.1, 0.2, 0.5, 1.0, 2.0, 3.0, and 5.0C, respectively. Upon returning to 1.0C, a high capacity of 166.1 mA h g^{-1} was recovered, indicating excellent reversibility and structural integrity. In contrast, the Li|PH-Li|NCM811 cell showed significantly lower capacities and poor rate recovery. The corresponding charge–discharge curves revealed two inclined voltage plateaus associated with the (de)lithiation of NCM811 (Fig. 5b and S28). Notably, the LSPH-based system showed minimal voltage hysteresis even under high-rate conditions. The cycling stability of both full cells at 1.0C is shown in Fig. 5c and d. The Li|LSPH|NCM811 cell maintained 70% capacity retention after 1000 cycles, demonstrating exceptional durability and interfacial stability consistent with observations in Li||Li symmetric cells. In contrast, the Li|PH-Li|NCM811 cell exhibited rapid capacity fading and increased voltage polarization during cycling at 1.0C (Fig. S29). The charge–discharge profiles of PH-Li at representative cycles show progressively distorted voltage plateaus and significantly enlarged overpotential from the 1st to the 300th cycle, indicating severe interfacial degradation. A direct comparison of both cells at corresponding cycles further confirms that the LSPH cell maintains stable voltage plateaus with minimal polarization growth, whereas the PH-Li cell suffers from continuous impedance increase, consistent with its inferior cycling stability (Fig. S30). Furthermore, after cycling, the charge-transfer resistance (R_{ct}) of the Li|PH-Li|NCM811 cell increased significantly, whereas only a minor change was observed for the Li|LSPH|NCM811 cell. This contrast indicates a much more stable electrode–electrolyte interface in the LSPH-based system (Fig. S31). When the cut-off voltage was increased to 4.5 V, the LSPH-based cell delivered a high initial capacity of 214 mA h g^{-1} and maintained 87.9% of its capacity after 100 cycles, with a coulombic efficiency exceeding 99% (Fig. 5e and f). These results highlight the synergistic effect between the zwitterionic filler and lithium salts, which enhances Li^+ transport kinetics and offers a new strategy for optimizing polymer electrolyte performance.

To further investigate the interfacial dynamics between the solid electrolyte and cathode, *in situ* impedance spectroscopy combined with the distribution of relaxation time (DRT) analysis was performed. As shown in Fig. 5g, impedance spectra were collected at different voltage stages during charge–discharge cycling at 0.1C. The DRT results resolved distinct relaxation processes. The peak observed in the 10^{-5} to 10^{-3} s range was assigned to the bulk resistance (R_0), whereas the peaks in the 10^{-3} to 10^{-1} s range were attributed to the anode–electrolyte interfacial resistance (R_{SEI}) and the cathode–electrolyte interfacial resistance (R_{CEI}).[34] Compared with the PH-Li system, the LSPH-based cell consistently exhibited lower R_{SEI} and R_{CEI} values, demonstrating faster Li^+ transport both within the bulk electrolyte and across the electrode–electrolyte interface.

This enhanced interfacial stability and reduced resistance are further corroborated by the microstructural characterization of the cycled NCM811 cathodes. High-resolution transmission electron microscopy (HRTEM) images (Fig. 5h) visually confirm that the NCM811 cathode cycled in the LSPH electrolyte features

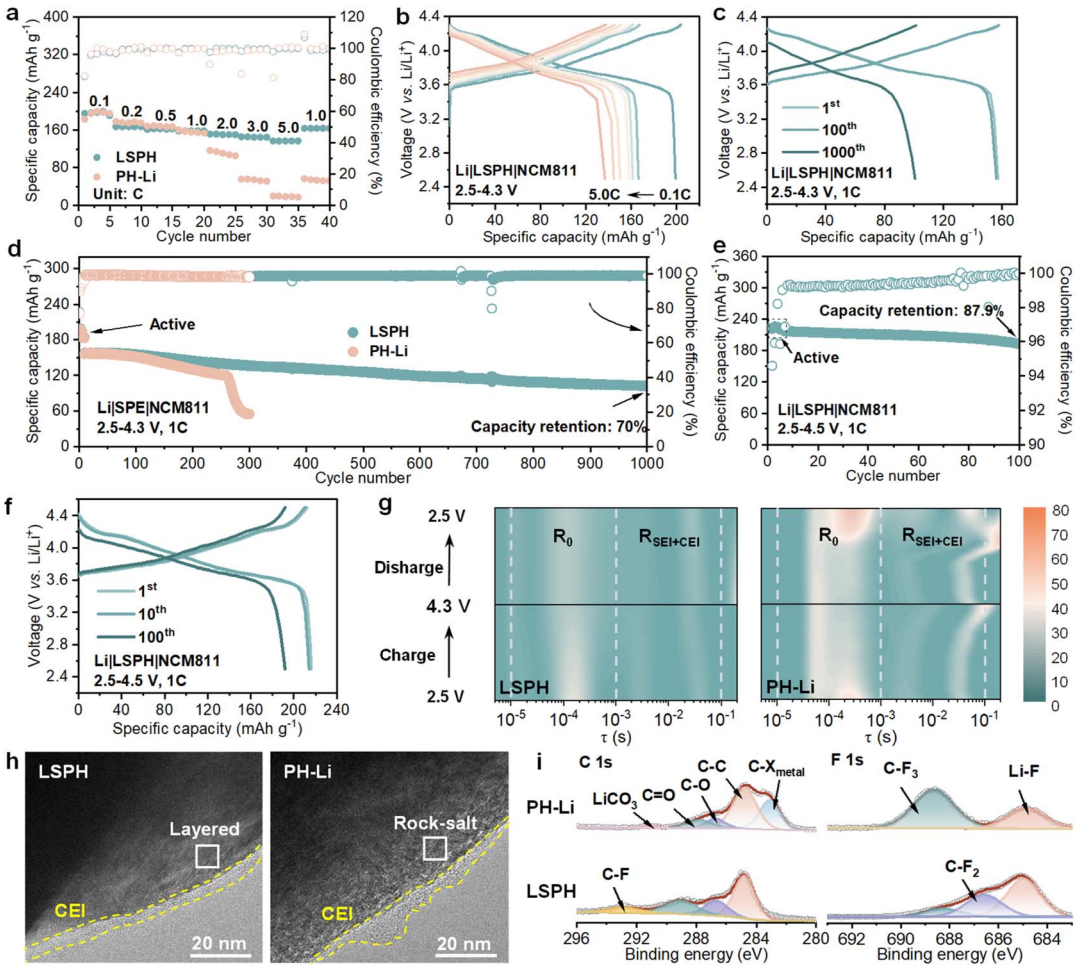

Fig. 5 Electrochemical performance of Li||NCM811 cells. (a) Rate performance with the LSPH and PH-Li electrolytes. Galvanostatic charge–discharge profiles of the cell with LSPH (b) at different rates and (c) at 1.0C. Cycling performance at (d) a 4.3 V cut-off voltage (comparing LSPH and PH-Li) and (e) a 4.5 V cut-off voltage (for LSPH). (f) Charge–discharge profiles of the cell with LSPH at 4.5 V. (g) DRT spectra for Li|LSPH|NCM811 and Li|PH-Li|NCM811 cells. (h) HRTEM images and (i) XPS C 1s and F 1s spectra of the cycled NCM811 cathodes using the LSPH and PH-Li electrolytes.

a thin, uniform, and robust CEI layer. Benefiting from this high-quality CEI, the highly ordered layered structure of the cathode is well-preserved at the near-surface region. In sharp contrast, the cathode cycled in the PH-Li system suffers from severe interfacial side reactions, leading to a thick, irregular CEI layer and obvious structural degradation from a layered phase to a disordered rock-salt phase at the surface. This structural preservation in the LSPH system effectively prevents the increase in charge transfer resistance during cycling.

C–X_{metal} bonds emerged in the C 1s spectrum of the NCM811 cathode cycled with the PH-Li electrolyte, indicating significant electrolyte decomposition at the NCM811 interface (Fig. 5i).[35] This might be attributed to the continuous decomposition of residual DMF, which compromised the interfacial stability. Moreover, a stronger LiF signal in the F 1s spectrum confirmed that the LSPH electrolyte promoted the formation of an anion-derived, inorganic-rich CEI, enhancing the interfacial stability. In summary, the incorporation of the LS filler reduces the residual DMF content, facilitates Li^+ transport through new conduction pathways, and promotes the formation of a compact, robust CEI. These effects alleviate structural degradation in the NCM811 cathode and significantly improve the long-term cycling stability of the solid-state Li|LSPH|NCM811 battery under ambient conditions.

Conclusions

In summary, a multifunctional zwitterionic metal–organic cage filler was designed and introduced into the PVDF-HFP matrix to weaken the dependence of Li^+ transport on residual solvents and stabilize the Li metal anode interface. The borate groups in the filler act as Li^+ donors that compete with DMF for coordination to form a weakly coordinated structure, while the Zn^{2+} centers immobilize $TFSI^-$. Together, these functions attenuate the strong Li^+–solvent coordination and lower the activation barrier for ion migration, leading to faster Li^+ transport and improved battery performance. Experimental analyses and AIMD simulations confirm that the zwitterionic filler effectively

reconstructs the Li^+ coordination structure, weakens Li^+–DMF/$TFSI^-$ interactions, and accelerates ion transport, thereby validating the proposed design strategy. As a result, the LSPH electrolyte achieves a high ionic conductivity of 0.641 mS cm^{-1}, a Li-ion transference number of 0.83, and an expanded electrochemical stability window up to 4.75 V. The Li|LSPH|Li symmetric cells deliver a high critical current density of 3.4 mA cm^{-2} and stable cycling for over 1000 h, accompanied by uniform lithium deposition and the formation of an inorganic-rich SEI. Furthermore, Li|LSPH|NCM811 full cell demonstrates excellent rate capability, delivering 136.3 mA h g^{-1} at 5C, and long-term cycling stability, maintaining 70% capacity retention over 1000 cycles at 1.0C and 4.3 V. Overall, this study proposes a promising strategy of regulating the Li^+ coordination environment with a multifunctional zwitterionic filler to overcome the limitations of VDF-based electrolytes, offering a generalizable approach to high-performance solid-state lithium metal batteries.

Author contributions

M. C. Z. and Z. G. L. contributed equally to this work. Y. Q. L., D. L. and M. R. W. conceived the idea and supervised the project. M. C. Z. and Z. G. L. designed the experiments and wrote the paper. M. C. Z. and Z. G. L. designed and drew the figures. M. C. Z. and Z. G. L. performed the experiments. Y. Y. L. performed the theoretical calculations. B. H., F. H. Y. and P. S. W. discussed the results and commented on the manuscript.

Conflicts of interest

There are no conflicts to declare.

Data availability

The data supporting this article are available within the article and its supplementary information (SI). Supplementary information: experimental details, materials synthesis and characterization, electrochemical measurements, theoretical calculation details, and figures and tables. See DOI: https://doi.org/10.1039/d6sc03303b.

Acknowledgements

This work was financially supported by the National Natural Science Foundation of China (No. 52574361), the Natural Science Foundation of Hunan Province (No. 2024JJ5425, 2025JJ20061), the Science and Technology Innovation Program of Hunan Province (No. 2023RC3054), a Project Supported by Scientific Research Fund of Hunan Provincial Education Department (No. 25B0017), Project of Yuelushan Center for Industrial Innovation (No. 2025YCII0134) and Central South University Research Program of Advanced Interdisciplinary Studies (No. 2023QYJC005). We thank the Beijing Fire Fly Star Shine Technology Limited Company for their assistance with the theoretical calculations.

Notes and references

1 H. Ji, J. Xiang, Y. Li, M. Zheng, L. Yuan, Y. Liao, L. Du, Z. Li, Z. Xie, K. Huang, X. Lin, Z. Xie, Y. Shen, M. Chen, T. Li, G. Feng, Y. Sun, L. Qie, H. Li, F. Zhang, R. Guo, X. Feng, W. Chen, X. Ai, J. Lu and Y. Huang, *Nature*, 2025, **643**, 1255–1262.
2 M. He, L. G. Hector, F. Dai, F. Xu, S. Kolluri, N. Hardin and M. Cai, *Nat. Energy*, 2024, **9**, 1199–1205.
3 H. Niu, N. Zhang, Y. Lu, Z. Zhang, M. Li, J. Liu, N. Zhang, W. Song, Y. Zhao and Z. Miao, *J. Energy Storage*, 2024, **88**, 111666.
4 Q. Xu, T. Li, Z. Ju, G. Chen, D. Ye, G. I. N. Waterhouse, Y. Lu, X. Lai, G. Zhou, L. Guo, K. Yan, X. Tao, H. Li and Y. Qiu, *Nature*, 2025, **637**, 339–346.
5 Z. Zhang and W.-Q. Han, *Nano-Micro Lett.*, 2023, **16**, 24.
6 W. Zhang, V. Koverga, S. Liu, J. Zhou, J. Wang, P. Bai, S. Tan, N. K. Dandu, Z. Wang, F. Chen, J. Xia, H. Wan, X. Zhang, H. Yang, B. L. Lucht, A.-M. Li, X.-Q. Yang, E. Hu, S. R. Raghavan, A. T. Ngo and C. Wang, *Nat. Energy*, 2024, **9**, 386–400.
7 Z. Song, F. Chen, M. Martinez-Ibañez, W. Feng, M. Forsyth, Z. Zhou, M. Armand and H. Zhang, *Nat. Commun.*, 2023, **14**, 4884.
8 X. Xie, P. Zhang, X. Li, Z. Wang, X. Qin, M. Shao, L. Zhang and W. Zhou, *J. Am. Chem. Soc.*, 2024, **146**, 5940–5951.
9 P. Ding, L. Wu, Z. Lin, C. Lou, M. Tang, X. Guo, H. Guo, Y. Wang and H. Yu, *J. Am. Chem. Soc.*, 2023, **145**, 1548–1556.
10 Y. Ren, S. Chen, M. Odziomek, J. Guo, P. Xu, H. Xie, Z. Tian, M. Antonietti and T. Liu, *Angew. Chem., Int. Ed.*, 2025, **64**, e202422169.
11 C. M. Costa, V. F. Cardoso, P. Martins, D. M. Correia, R. Gonçalves, P. Costa, V. Correia, C. Ribeiro, M. M. Fernandes, P. M. Martins and S. Lanceros-Méndez, *Chem. Rev.*, 2023, **123**, 11392–11487.
12 P. Shi, J. Ma, M. Liu, S. Guo, Y. Huang, S. Wang, L. Zhang, L. Chen, K. Yang, X. Liu, Y. Li, X. An, D. Zhang, X. Cheng, Q. Li, W. Lv, G. Zhong, Y.-B. He and F. Kang, *Nat. Nanotechnol.*, 2023, **18**, 602–610.
13 Q. Wu, M. Fang, S. Jiao, S. Li, S. Zhang, Z. Shen, S. Mao, J. Mao, J. Zhang, Y. Tan, K. Shen, J. Lv, W. Hu, Y. He and Y. Lu, *Nat. Commun.*, 2023, **14**, 6296.
14 D. Zhang, Y. Liu, S. Yang, J. Zhu, H. Hong, S. Li, Q. Xiong, Z. Huang, S. Wang, J. Liu and C. Zhi, *Adv. Mater.*, 2024, **36**, 2401549.
15 X. Zhang, J. Han, X. Niu, C. Xin, C. Xue, S. Wang, Y. Shen, L. Zhang, L. Li and C. W. Nan, *Batter. Supercaps*, 2020, **3**, 876–883.
16 X. Chang, R. Cheng, T. Wang, X. Kan, M. Jia, Z. Bi, X. Fan and X. Guo, *Energy Environ. Sci.*, 2025, **18**, 9490–9501.
17 B. Sheng, J. Lu, H. Chen, Q. Fang, W. Ding, M. Chen, J. Chen, X. Wang, G. Zhong, X. Han and Z. Peng, *Adv. Funct. Mater.*, 2025, **36**, e14960.
18 Q. Liu, G. Yang, X. Li, S. Zhang, R. Chen, X. Wang, Y. Gao, Z. Wang and L. Chen, *Energy Storage Mater.*, 2022, **51**, 443–452.

19 M. Li, H. An, Y. Song, Q. Liu, J. Wang, H. Huo, S. Lou and J. Wang, *J. Am. Chem. Soc.*, 2023, **145**, 25632–25642.
20 W. Yang, Y. Liu, X. Sun, Z. He, P. He and H. Zhou, *Angew. Chem., Int. Ed.*, 2024, **63**, e202401428.
21 Y. Li, W. Yuan, Z. Hu, Y. Shen, G. Wu, F. Cong, X. Fu, F. Lu, Y. Li, P. Liu, Y. Huang and J. Li, *Adv. Funct. Mater.*, 2025, **35**, 2424763.
22 D. Liu, M. Chen, K. Li, Z. Li, J. Huang, J. Wang, Z. Jiang, Z. Zhang, T. Xie, G. R. Newkome and P. Wang, *J. Am. Chem. Soc.*, 2020, **142**, 7987–7994.
23 P. H. Duan, J. L. Yu, Q. S. Liu, G. Wu, X. L. Wang and Y. Z. Wang, *Adv. Funct. Mater.*, 2024, **34**, 2402065.
24 P.-H. Duan, G.-R. Zhu, J.-L. Yu, Z. Guan, Y. Gao, G. Wu, X.-L. Wang and Y.-Z. Wang, *J. Mater. Chem. A*, 2025, **13**, 9111–9119.
25 Y. Ma, Y. Qiu, K. Yang, S. Lv, Y. Li, X. An, G. Xiao, Z. Han, Y. Ma, L. Chen, D. Zhang, W. Lv, Y. Tian, T. Hou, M. Liu, Z. Zhou, F. Kang and Y.-B. He, *Energy Environ. Sci.*, 2024, **17**, 8274–8283.
26 K. Wang, V. Koverga, N. Maslekar, F. Wu, R. Kuphl, X. Lyu, P. Deshpande, H. Guo, H. Seol, W. Degraff, J. L. Schaefer, C. Fang, T. Li, G. Cheng, A. T. Ngo and S. Kim, *Adv. Energy Mater.*, 2025, **15**, 2405676.
27 M. Guo, S. Gao, Y. Wang, K. Liu, J. Zhao, Z. Zhang, Y. Li, C. Li and L. Zhang, *Adv. Funct. Mater.*, 2025, **36**, e09739.
28 K. Yang, J. Ma, Y. Li, J. Jiao, S. Jiao, X. An, G. Zhong, L. Chen, Y. Jiang, Y. Liu, D. Zhang, J. Mi, J. Biao, B. Li, X. Cheng, S. Guo, Y. Ma, W. Hu, S. Wu, J. Zheng, M. Liu, Y.-B. He and F. Kang, *J. Am. Chem. Soc.*, 2024, **146**, 11371–11381.
29 Z. Piao, X. Wu, H.-R. Ren, G. Lu, R. Gao, G. Zhou and H.-M. Cheng, *J. Am. Chem. Soc.*, 2023, **145**, 24260–24271.
30 Y. Zhai, Y. Zhang, N. Wang, M. Li, M. Shen, P. Xu, M. Sun, F. Dong, T. Ma, J. Ming, L. Cong, H. Xie and Y. Liu, *Energy Environ. Sci.*, 2025, **18**, 8352–8365.
31 Z. Li, H. Wang, Y. Zheng, Y. Zhu, B. Qin, Z. Lu, W. Yan and J. Zhang, *Angew. Chem., Int. Ed.*, 2025, **64**, e202508857.
32 T. Ma, B. Fu, H. Feng, Y. Li, Y. Zhai, Y. Tian, Z. Li and Z. M. Su, *Angew. Chem., Int. Ed.*, 2025, **64**, e202501412.
33 D. Zhang, Y. Liu, D. Li, S. Li, Q. Xiong, Z. Huang, S. Wang, H. Hong, J. Zhu, H. Lv and C. Zhi, *Energy Environ. Sci.*, 2025, **18**, 227–235.
34 M. Li, Y. Chen, S. Wu, W. Wang, J. Zhou, Q. Fu, P. Xiao and J. Liu, *Angew. Chem., Int. Ed.*, 2025, **64**, e202514299.
35 W. Zhang, Y. Lu, Q. Feng, H. Wang, G. Cheng, H. Liu, Q. Cao, Z. luo, P. Zhou, Y. Xia, W. Hou, K. Zhao, C. Du and K. Liu, *Nat. Commun.*, 2025, **16**, 3344.